Catalytic Mechanism and Allosteric Regulation of UDP-Glucose Pyrophosphorylase from *Leishmania major*

Jana Führing,[†] Johannes T. Cramer,[†] Françoise H. Routier,[†] Anne-Christin Lamerz,[†,⊥] Petra Baruch,[‡] Rita Gerardy-Schahn,[†] and Roman Fedorov[‡,§,*]

[†] Institute for Cellular Chemistry, OE4330, Hannover Medical School, Carl-Neuberg-Strasse 1, 30625 Hannover, Germany
[‡] Research Division for Structural Analysis, OE8830, Hannover Medical School, Carl-Neuberg-Strasse 1, 30625 Hannover, Germany
[§] Institute for Biophysical Chemistry, OE4350, Hannover Medical School, Carl-Neuberg-Strasse 1, 30625 Hannover, Germany

Ⓢ Supporting Information

ABSTRACT: UDP-glucose pyrophosphorylase (UGP) is a nucleotidyl-transferase of central importance in all organisms and considered an attractive drug target in the human pathogens *Leishmania* and *Trypanosoma*. Here, we used wild-type and mutant *Leishmania major* UGP to solve the crystal structures of postreactive, UTP, and UDP-Glc bound states and performed kinetic and theoretical chemistry analysis of the enzymatic reaction. The new data filled critical gaps in the knowledge of the UGP mechanism and allowed reconstructing the complete enzymatic cycle on three levels: global (movements of molecular functional blocks), local (behavior of separate residues), and chemical (quantum mechanical description of enzymatic reaction).

Results were integrated into a model of UGP activity describing structural changes along the cycle, the mechanisms of substrate binding, UGP catalysis, and product release. Our study revealed the mechanisms of allosteric regulation common for nucleotidyltransferases and, in particular, the mechanical control of the chemical reaction in the active site.

KEYWORDS: nucleotidyltransferase, catalysis, allosteric regulation, molecular mechanism, Leishmania, Trypanosoma, complete enzymatic cycle, mechanochemistry
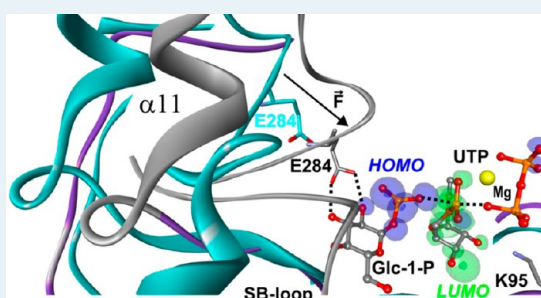
■ INTRODUCTION

Enzymes of the large superfamily of nucleotidyltransferases (nucleotide triphosphate (NTP) transferases) catalyze key cellular processes in all kingdoms of life.[1] Within the wide spectrum of functions, members of this superfamily are responsible for DNA repair, RNA editing, and activation of metabolites used in catabolic pathways, as well as detoxification and antibiotic resistance mechanisms.[1] Despite large diversity existing at primary and quaternary structure levels (mono-, di-, tetra-, hexa-, and octameric forms have been described[2−6]), nucleotidyltransferases commonly adopt Rossmann-like $\alpha/\beta/\alpha$ sandwich folds in their catalytic domains,[6] require Mg^{2+} for catalytic activity,[7−9] and follow an ordered sequential Bi Bi catalytic mechanism, with the NTP binding first.[4,5,10,11] In keeping with their central cellular positions, nucleotidyltrans-ferases have been demonstrated to be a subject of elaborate regulatory mechanisms,[1] including allosteric effectors, redox regulation, phosphorylation[12−15] and sequestration of active enzymes by oligomerization.[3,16] Although intensively studied at both the kinetic and structural levels,[4,5,10,11] molecular details explaining common functional properties of nucleotidyltrans-ferases, such as the bireactant kinetics and the role of the essential Mg^{2+} ion, are either missing or equivocally discussed.[7,10] Similarly, it remains unknown how the various levels of structural organization combine with allosteric

regulation to affect the reaction cycles of these enzymes. Elucidating these mechanisms is, however, essential for the fundamental understanding of nucleotidyltransferases and the development of new concepts to specifically inhibit individual members.

Recently, we cloned UDP-glucose (UDP-Glc) pyrophos-phorylase from *Leishmania major* (LmUGP).[2] This enzyme catalyzes the reversible conversion of glucose-1-phosphate (Glc-1-P) and uridine 5′-triphosphate (UTP) to UDP-Glc and inorganic pyrophosphate (PP_i) in the presence of Mg^{2+} ions. Very different from all known pro- and eukaryotic UGPs, the LmUGP is an active monomer with no capability to form higher oligomers that, for example, in plants represent sequestered enzyme forms.[3,16] This unique feature together with the fact that UGP is a promising target for the development of specific antiparasitic agents[17,18] motivated us to investigate the function of this enzyme at the macro-molecular, atomic, and chemical levels.

Previously obtained open and closed structures of LmUGP (pdb codes: 2OEF and 2OEG, respectively) revealed major conformational change between these two states.[19] To
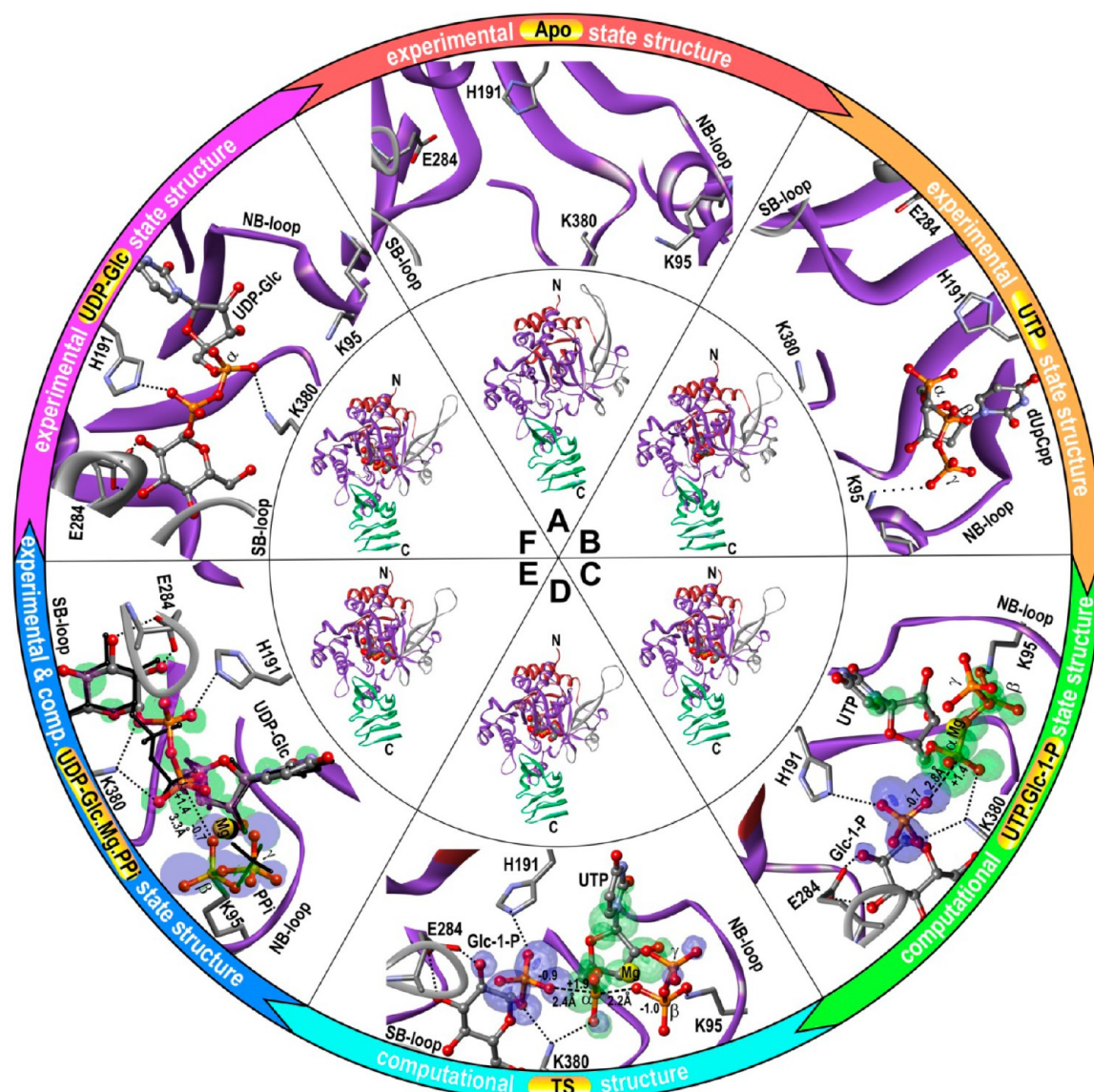
Figure 1. Enzymatic cycle of LmUGP. The inner circle shows the overall views of LmUGP for each state in ribbon representation. The outer circle shows the close-ups of the UGP active site. The N-terminal, C-terminal, and central catalytic domains are shown in red, green, and purple, respectively. The lock region is shown in gray. The substrates are shown in a Corey−Pauling−Koltun representation. The outer segments C, D, and E contain graphical representations of HOMO (blue) and LUMO (green). Only lobes of the same sign localized on reacting atoms are shown. (A) Open state (apo form) representations based on the experimental structure 2OEF.[19] The N-terminal/catalytic and C-terminal domains are at their maximum distance, the seven-stranded β-sheet is relaxed, the lock is open. Only the binding site for UTP is present. (B) Crystal structure of LmUGP·dUpCpp complex representing the UTP state. The seven-stranded β-sheet and the NB loop acquire intermediate conformations between the open and the closed states, and the lock region remains open. The phosphates are located in the interface between the catalytic and C-terminal domains with the γ-phosphate stabilizing the NB loop. The binding pocket for the glucose ring is formed. (C) QM/MM model of the prereactive state. The whole structure is in the closed state; both substrates are stabilized in position for the reaction. (D) The trigonal bipyramidal geometry of the transition state. (E) QM/MM (colored) and experimental (black) models of the postreactive state. (F) Experimental structure of UDP-Glc state (2OEG).[19] The pyrophosphate dissociation leads to the relaxation of the NB loop and the activation of the lock mechanism for opening the LmUGP structure.

understand these molecular movements and reconstruct a comprehensive picture of the enzymatic cycle, we aimed to obtain additional intermediate state geometries. Here, we determined the crystal structures of wild-type and mutant LmUGP in the presence of substrates, products, or their analogs.

The new structures for the first time revealed the binding sites for all UGP products, elucidated the key role of the UTP nucleoside and γ-phosphate in UGP activation, and helped explain the allosteric mechanisms that accompany binding and

stabilization of both substrates of the bireactant LmUGP. Moreover, novel insights into the elements responsible for substrate binding and product release have been obtained. Our structural analysis is supported by original kinetics data presented in this study and by published data for the forward and backward reactions of the wild-type LmUGP and its functional mutants.[2,19] The ab initio quantum mechanics/molecular mechanics (QM/MM) calculations of the LmUGP reaction pathway helped elucidate electronic effects and the roles of Mg^{2+} and active site residues in UGP catalysis.
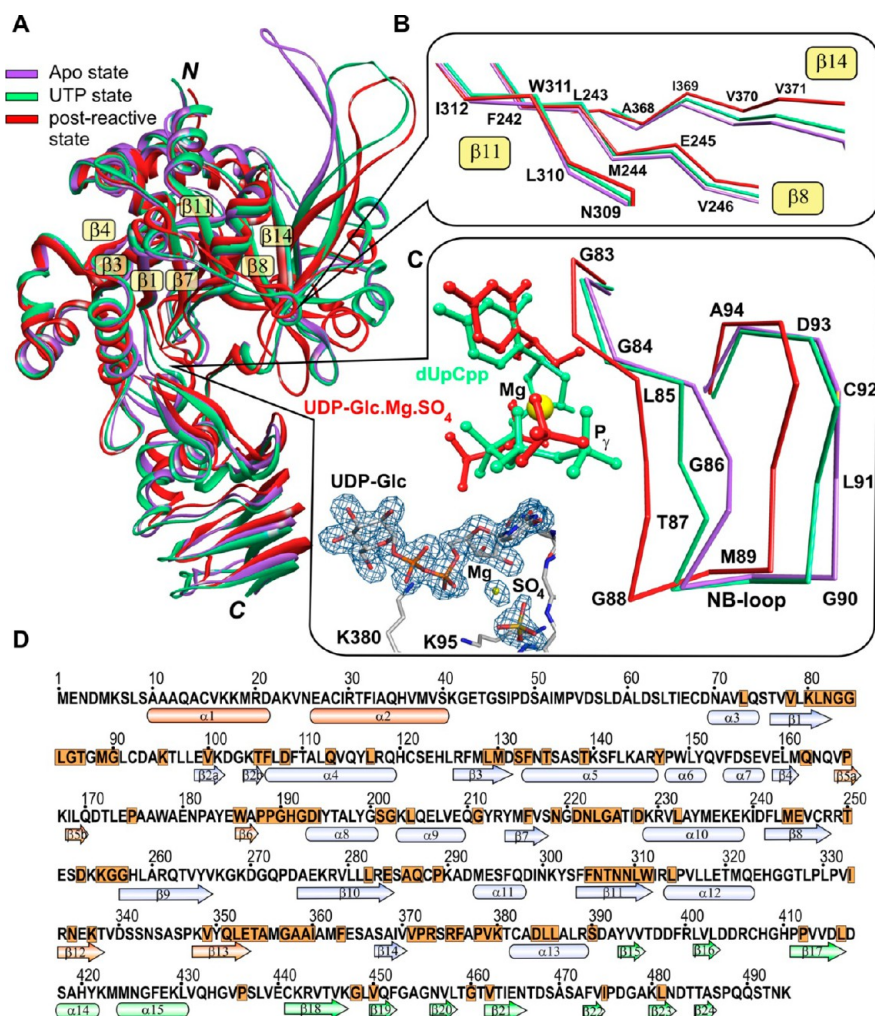
Figure 2. (A) Superposition of the LmUGP structures in the apo state (purple; PDB code: 2OEF[19]), the UTP state (green; LmUGP·dUpCpp complex), and the postreactive state (red; LmUGP·UDP-Glc·Mg^{2+}·SO$_4$ complex) illustrates the overall conformational changes upon binding the first and second substrates. The torsional deformation of the seven-stranded β-sheet in the area near the glucose binding site is shown in panel B. Panel C shows structural changes in the NB loop area and the $F_{obs} - F_{calc}$ electron density omit map contoured at 3.0 σ around the ligands UDP-Glc, Mg^{2+} and SO$_4^{2-}$ in the wild-type LmUGP postreactive state structure. (D) Amino acid sequence of LmUGP. The secondary structure elements of the N-terminal domain are red; catalytic domain, blue; and C-terminal domain, green.[19] The residues conserved in UGPs from different organisms are highlighted in orange.

The resulting model of UGP activity describes structural changes along the catalytic cycle, the mechanisms of substrate binding, UGP catalysis, and product release (Figure 1). With this description of the complete reaction cycle of LmUGP, we provide novel insights into the function of nucleotidyltransferases and a general guide for the in-depth mechanistic analysis of these enzymes. Finally, we demonstrate how allosteric mechanisms control specific recognition of glucose by LmUGP and regulate the chemical reaction in the active site via mechanical force transduction.

■ EXPERIMENTAL SECTION

Protein Preparation and Crystallization. Untagged and C-terminally His$_6$-tagged wild-type *L. major* UGP were prepared as described by Lamerz et al.[2] Mutant proteins L281D and H191L were prepared as described by Steiner et al.[19] The E284A mutant was created by overlap extension PCR using mutagenesis primers with the sequences gctgcggGCGtccgc (sense) and gcggaCGCccgcagc (antisense), respectively, in which the mutated codon is given in uppercase.

The C-terminally His$_6$-tagged E284A mutant protein was then expressed and purified in the same way as the His$_6$-tagged wild-type protein.[2] Crystals of the wild-type enzyme complexes were grown at 20 °C by vapor diffusion in hanging drop geometry with 500 μL of reservoir solution. Crystals of the L281D and the H191L mutants were grown at 4 and 20 °C, respectively, in sitting drop geometry with 500 μL of reservoir solution. For the UTP state, 1 mM dUpCpp and 4 mM MgCl$_2$ were added to the wild-type protein (12.4 mg/mL; 10 mM Tris−HCl, pH 7.5; 100 mM NaCl; 2 mM MgCl$_2$; 2 mM DTT). A 1.0 μL portion of the resulting complex was mixed 1:1 with the reservoir solution (0.1 M MES, pH 6.4; 20% w/v PEG-4000; 200 mM Li$_2$SO$_4$). For the postreactive state, 1.1 μL of the wild-type protein (7 mg/mL; 10 mM Tris−HCl, pH 7.5; 100 mM NaCl; 2 mM MgCl$_2$; 2 mM DTT; 4 mM UDP-Glc) was mixed 1:1 with the reservoir solution (0.1 M Bis-Tris, pH 6.0; 22% w/v PEG-MME-2000; 20 mM (NH$_4$)$_2$SO$_4$). The L281D mutant was concentrated to 2.3 mg/mL in the same buffer adjusted to pH 7.8. The reservoir solution contained 0.1 M Bis-Tris, pH 6.6, and 28% w/v PEG-MME-2000. In the case of the H191L

mutant, the protein buffer contained 10 mg/mL LmUGP$_{H191L}$; 10 mM Tris−HCl, pH 7.5; 100 mM NaCl; 2 mM MgCl$_2$; 2 mM DTT; 4 mM UTP; and 4 mM Glc-1-P. The reservoir solution contained 10% v/v glycerol; 0.05 M citrate buffer, pH 5.2; and 1.1 M sodium citrate. Prior to flash-cooling, all crystals were rinsed in reservoir solution supplemented with 20% ethylene glycol for cryoprotection.

In Vitro Activity Measurements and Kinetic Data Analysis. To calculate reaction energy parameters, the in vitro activity of wild-type LmUGP was measured at 25 and 37 °C using the untagged recombinant protein. In the forward direction of the reaction (production of UDP-Glc), formation of pyrophosphate was continuously detected using the EnzChek Pyrophosphate Assay Kit (Molecular Probes) in a buffer containing 50 mM Tris/HCl, pH 7.8, and 10 mM MgCl$_2$. UTP was kept at a saturating concentration of 1 mM, and the concentration of Glc-1-P was varied between 0.1 and 3 mM. The backward reaction (formation of UTP) was monitored using the continuous assay described by Damerow et al.[20] Here, UDP-Glc was supplied at a saturating concentration of 1 mM, and pyrophosphate concentration was varied between 0.1 and 2 mM. For the forward and backward reaction activity assays, a 1.84 mg/mL UGP stock was diluted 1:40 000 and 1:10 000, respectively. The reaction was started by addition of 10 μL of diluted UGP unto a final reaction volume of 100 μL. The resulting values of $[E]_0$ for the forward and backward reactions were 8.6915×10^{-11} M and 3.4766×10^{-10} M, respectively. Product formation was continuously monitored at 360 nm in a microplate reader (Power-Wave 340 KC4 system, Bio-Tek). The rates of product release were plotted against the varied substrate concentration, and K_m and V_{max} were calculated using the nonlinear fitting function in PRISM software (GraphPad Software, Inc.). The free-energy barriers resulting from the experimental V_{max} values (Supporting Information Figure S2A,B) were calculated assuming that the reaction catalyzed by LmUGP proceeds via the ordered sequential Bi Bi catalytic mechanism common for nucleotidyltransferases, with a single barrier between the pre- and postreactive states. In this case, the rate-limiting step constant corresponding to the substrate-to-product conversion is identical to $k_{cat} = V_{max}/[E]_0$, and the reaction free energy barrier can be estimated according to the transition state theory (TST) as $\Delta G^{\#} = -RT \ln(k_{cat}h)/(k_BT)$, where R, k_B, and h are the ideal gas, Boltzmann's, and Planck's constants, respectively, and T is the absolute temperature.

To compare kinetic parameters of the LmUGP E284A mutant and wild-type LmUGP (both C-terminally His-tagged), activity measurements at 25 °C in the forward direction of the reaction were carried out and evaluated as described above, with the following modifications: UTP concentration was varied between 0.05 and 1 mM at a saturating supply of 2 mM Glc-1P, and titration of Glc-1P between 0.05 and 2 mM was performed at a saturating concentration of 1 mM UTP.

Diffraction Data Collection and Structure Determination. Diffraction data were collected at the EMBL beamlines X11 and X13 at the DORIS storage ring, DESY, Hamburg, and the beamlines ID23-2 and ID29, at ESRF, Grenoble, using MAR CCD and Dectris Pilatus 6 M detectors (see Supporting Information Table S1 for details), and reduced with the XDS program package.[21] The structures of LmUGP$_{wt}$·dUpCpp complex and LmUGP$_{H191L}$ mutant was solved by molecular replacement (CCP4 software suite[22,23]) using the structure of LmUGP apo form (pdb code: 2OEF[19]) as an initial model.

Structure determination of LmUGP$_{wt}$·UDP-Glc·Mg^{2+}·SO$_4$ and LmUGP$_{L281D}$·UDP-Glc complexes was initiated by a round of CNS[24,25] rigid body refinement using the protein part of the LmUGP coordinates for the closed conformation of the enzyme (pdb code: 2OEG[19]) as an initial model. Refinement was continued with CNS, SHELX,[26] and REFMAC[27] and included simulated annealing and individual B-factor refinement. The initial electron density maps were calculated using ARP/wARP.[28] During cyclic rounds of refinement and manual rebuilding using the COOT[29] program, ligands and solvent molecules were included in the models (see Figures 2C and Supporting Information S1A−D). The final models displayed good stereochemistry (see Supporting Information Table S1). Structure comparisons were performed using SSM and LSQ superpose tools of COOT.

Molecular Dynamics Simulations. To study the effect of the E284−glucose interaction on the conformation of LmUGP, molecular dynamics (MD) simulations were performed using the CNS[24,25] program package. The starting geometry was obtained from the coordinates of the LmUGP$_{wt}$·dUpCpp complex (UTP state) and the glucose coordinates from the superimposed structure of the LmUGP$_{wt}$·UDP-Glc·Mg^{2+}·SO$_4$ complex (postreactive state). In this geometry, the distances between the oxygen atoms of the E284 carboxyl group and the 2′,3′-oxygen atoms of glucose were close to 6 Å. At the start of the simulations, the hydrogen bond distance restraints between these atoms were assigned. The Cartesian MD simulations were performed for 1 ns MD trajectory at a constant temperature of 300 K. At the end of the dynamic trajectory, the model geometry was optimized using CNS-DEN refinement[30] without experimental energy terms.

Quantum Chemical Modeling of LmUGP Reaction Pathway. The QM/MM simulations of the LmUGP reaction pathway were performed using the Firefly Quantum Chemistry package,[31] based in part on the GAMESS (US)[32] source code. The QM subsystem included the substrates, water, Mg^{2+}, and fractions of the side chains for the protonated residues K95, H191, and K380. It contained 94 atoms in total and had a charge of −1. The rest of the protein was included into the MM part. Geometry optimizations, Hessian calculations, saddle point location, and intrinsic reaction coordinate (IRC) simulations in the QM part were carried out using density functional theory (DFT) with the B3LYP hybrid functional,[33,34] Vosko−Wilke−Nusair electron gas formula 5 correlation,[35,36] and the valence double-ζ polarized basis set 6-31G* for all atoms. The MM3 force field parameters[37−39] were used for the MM part. The starting geometry for the saddle point location search was generated from the coordinates of the postreactive state complex and the substrate coordinates from the structure of LmUGP·dUpCpp complex obtained in this work. This structure was optimized using an unconstrained QM/MM geometry minimization procedure.

The search for the saddle point location was started by successively decreasing the distance between the reacting atoms $O_{3P}{}^{Glc-1-P}$ and $P_\alpha{}^{UTP}$ in the direction of the forward reaction and performing constrained geometry minimization at each step. Upon reaching the flat conformation of the $P_\alpha O_3$ group of UTP, the precise location search of the saddle point was performed using a quadratic approximation augmented Hessian technique.[40−42] The transition state geometry was located at a point with a single imaginary frequency of Hessian. After finding the transition state, the structures of the pre- and postreactive states were obtained by descent forward and

backward from the saddle point along the steepest descent path in mass-weighted Cartesian coordinates using the IRC method.[43] The resulting models of pre- and postreactive states corresponded to the true minima on the potential energy surface with all real vibrational frequencies. These structures were used for further analysis and comparison with experimental data. The free energy barriers for forward and backward reactions were calculated using harmonic normal mode approximation.

■ RESULTS

LmUGP·dUpCpp Complex and the Mechanism of UTP Binding. To study the effect of UTP-binding on the structure and function of LmUGP, we crystallized LmUGP in the presence of the nonreactive UTP analog dUpCpp (see Experimental Section for details). The structure solved by molecular replacement and refined to 3.0 Å resolution showed good electron density for the UTP analog bound to the active site (Supporting Information Figure S1C). The overall conformation of the enzyme is more similar to the open[19] than to the closed (postreactive; see below) state, with several regions acquiring intermediate conformations (Figure 2A). Compared with the open state, the large magnitude change is located in the nucleotide-binding (NB) loop, which shifts 2.4 Å toward the phosphate moiety, bounding the nucleotide pocket (Figure 2C). The seven-stranded β-sheet (β1, β3, β4, β7, β8, β11, β14; Figure 2D) undergoes a torsional deformation, where strands β1, β7, β8 (and adjacent region of the helix α10), β11, and β14 shift toward their positions in the closed state (Figure 2B), while the conformation of β3 and β4 remains close to the open state. The nucleoside is coordinated by residues L81, G83, G84 (NB loop), M130 (β3), Q162 (end of β4), G190-H191 (loop β6−α8), and N219−D221 (end of β7). Most of these residues remain structurally conserved in the open, UTP, and closed states of the enzyme, which explains why UTP can bind to the apo form and activate the conformational transition. To understand the role of nucleoside binding in LmUGP activation, we crystallized the inactive LmUGP mutant H191L[19] in the presence of both UTP and Glc-1-P, but no electron density was observed for the substrates. Instead, the mutant structure revealed that the side chain of L191 occupied part of the space necessary for the nucleoside binding (Figure 3C). As a result, UTP could not bind, and the mutant conformation remained very close to the open form of the wild-type protein. This finding supported the primary role of the nucleoside binding in UGP activation.

In the X-ray structure of the LmUGP·dUpCpp complex, the phosphates of the UTP analog were coordinated by the residues in the interface between the catalytic and C-terminal domains. It is interesting that in this state, the strictly conserved residue K380, known to interact with the product UDP-Glc and to be essential for enzymatic activity,[19] is located 8 Å away from the α-phosphate and does not make any interaction with the phosphate moiety (Figure 1B). The γ-phosphate forms three hydrogen bonds and several van der Waals interactions with the NB loop residues G84−T87 and a salt bridge with the strictly conserved K95. These interactions explain the large shift of the NB loop upon UTP binding. As the NB loop, in turn, is bound to the C-terminal domain via a hydrogen bond and extensive hydrophobic contacts, the new structural data elucidate the role of the γ-phosphate in the mechanism of UGP activation.

Glucose-1-phosphate Binding to LmUGP. As typical in enzymes with ordered sequential Bi Bi kinetics, the binding site
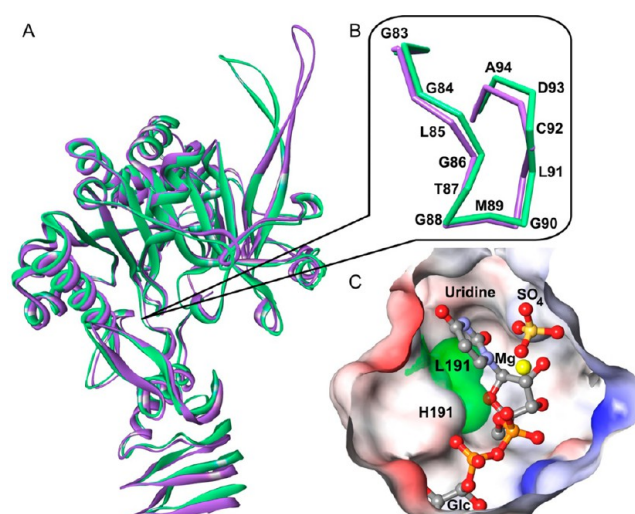

Figure 3. Structural effects of H191L mutation. Superposition of the wild-type LmUGP structure in the apo state (pdb code: 2OEF;[19] green) and LmUGP$_{H191L}$ mutant crystallized in the presence of both substrates (purple) shown for the whole enzyme (A) and for the NB loop area (B). (C) Superposition of the substrate binding pocket in the postreactive state of LmUGP$_{wt}$ and in the LmUGP$_{H191L}$ mutant structure. The color scheme of the wild-type protein surface corresponds to the atom charge (blue, positive; red, negative; white, neutral). The van der Waals surface of L191 from the superimposed LmUGP$_{H191L}$ mutant structure is shown in green.

for Glc-1-P does not exist in the apo form of LmUGP. The residues N219 (β7), N306−N308 (β11), and F376 (link β14−α13), identified as responsible for glucose binding in the closed LmUGP structure,[19] overlap with the atoms of the glucose ring in both our postreactive state and UDP-Glc[19] complexes. In the UTP state, these residues are shifted deeper into the catalytic domain as a result of the torsional deformation of the seven-stranded β-sheet, which removes steric hindrances and creates a complementary surface for the glucose ring. This, together with the fact that Glc-1-P binding cannot occur without UTP binding first, as demonstrated by STD-NMR studies,[2] implies that the binding of the glucose ring must play a primary role in the binding of Glc-1-P. Thus, the UTP-induced deformation of the β-sheet is an important determinant of the Glc-1-P binding site formation.

Other structural elements known to contribute to the glucose binding in the above-mentioned closed LmUGP structures include the highly conserved sugar-binding (SB) loop and the strictly conserved residue E284 located at the end of β10 (Figure 2D). These residues belong to a larger region R249−Y302 comprising the SB loop, the adjoining β-hairpin β9−β10 (handle) and helix α11. Superposition of LmUGP structures showed that this region changes dramatically between the open and closed states (Figure 2A). Surprisingly, in the UTP-state structure, the conformation of this region remains almost identical to the open state, with the exception of the top part of the handle, which is known to be flexible, as indicated by the experimental electron density.

In the UTP state, both the SB loop and E284 are distanced from the glucose binding site, but E284 is located 2.0 Å closer than the nearest SB loop residue and, therefore, can bind first. To study the structural effect of the interaction between E284 and the glucose ring, we have performed molecular dynamics simulations (see Experimental Section for details). As a starting model, we used the structure of the LmUGP$_{wt}$·dUpCpp

complex (UTP state) and the glucose coordinates from the superimposed structure of the $LmUGP_{wt} \cdot UDP\text{-}Glc \cdot Mg^{2+} \cdot SO_4$ complex (closed postreactive state, see below). During these simulations, the force was applied to the side chain of E284 to bring it to its position in the closed state of the enzyme. E284 is linked to the SB loop via the β-hairpin structure of the handle and our molecular dynamics simulations suggested that pulling E284 in the direction of the glucose-binding site results in the movement of the whole region R249−Y302 toward its conformation in the closed state.

To test this hypothesis, we first examined the role of E284 in glucose binding. Therefore, mutant E284A was constructed and kinetically characterized in comparison with the wild-type enzyme (Supporting Information Figure S2C,D). The specific activity of the mutant E284A was reduced to less than 0.05% of the wild-type. By measuring K_m values, the affinity of the E284A mutant for UTP was found to be nearly unchanged (E284A, 73.9 ± 5.8 μM versus wt, 101.2 ± 7.6 μM), whereas the affinity for Glc-1-P was drastically impaired (E284A, 977.4 ± 99.5 μM versus wt, 152.8 ± 14.3 μM).

To study the interaction between E284 and the SB loop, we investigated structural effects of the L281D mutation located in the link connecting these two areas, at the end of the strand $\beta10$. L281 forms a part of the hydrophobic core stabilizing the base of the handle and its contact with the N-terminal and catalytic domains. The L281D mutation leads to a drop of specific activity (measured in the forward reaction) to 16.3% of the wild type.[19] Because the residue is spatially remote from active site and SB loop, the mechanism of this inactivation was previously unclear. The crystal structure of the L281D mutant in complex with UDP-Glc solved in this study now shows that the mutation leads to a disruption of the β-structure of the handle (Figure 4A) and an increase in its flexibility, reflected in the weakening of experimental electron density for this region. In the mutant structure, the interactions between E284 and glucose are not changed, but the distances between E284 and the SB loop or $\alpha11$ are increased, and a lack of closure is observed in both the SB loop and the $\alpha11$ area (Figure 4B). Thus, the disruption of the β-structure caused by the L281D mutation leads to the loss of stiffness in the handle and, therefore, a reduction of its efficiency in transducing tensile force to the SB loop and $\alpha11$. This, in its turn, leads to a lack of closure in these areas (Figure 4B) and a decrease in the specific activity of the L281D mutant to 16.3% of the wild-type enzyme.[19] The top of the handle features significant conformational flexibility observed in the crystal structures of LmUGP, and its length varies between species. This, in conjunction with the observed effect of the L281D mutation, implies that the residues involved in transduction of the tensile force are located at the base of the handle.

Comparison of the UTP state and closed postreactive state structures showed that closing the region R249−Y302 brings the strictly conserved residues H191 and K380 in a favorable position for binding Glc-1-P phosphate and leads to adjustments in the glucose binding site that further increase its complementarity. After closing, the region R249−Y302 is additionally stabilized by a hydrogen bond between the SB loop E251 and the C-terminal domain R443 observed in the closed state structures.

Product Formation and Allosteric Regulation of Product Release. By cocrystallizing LmUGP with UDP-Glc, Mg^{2+}, and SO_4^{2-} ions, the postreactive state of the enzyme could be trapped, and the structure, resolved to the high
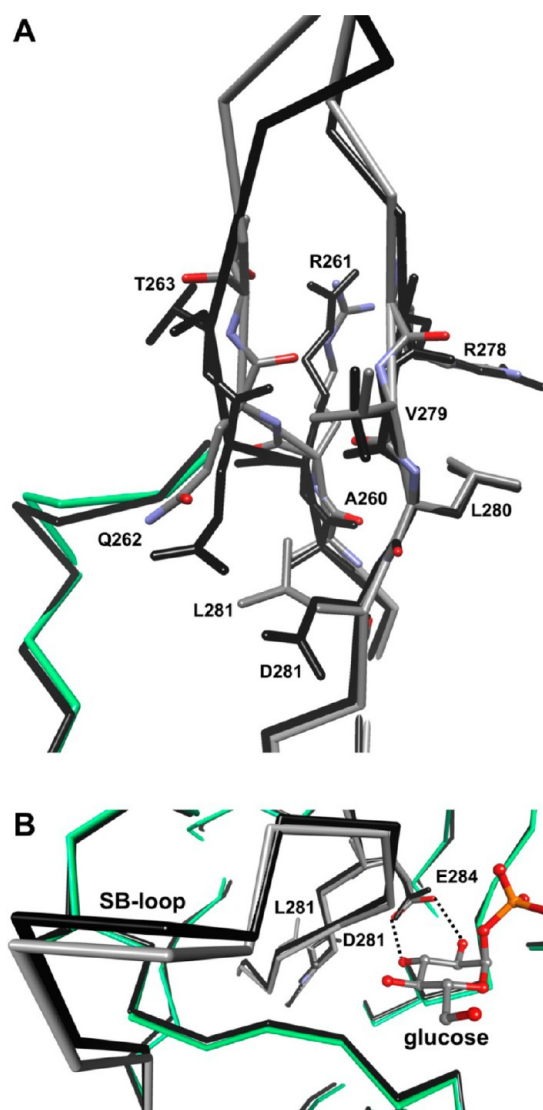

Figure 4. Superpositions of the wild-type (colored) and L281D mutant (black) LmUGP·UDP-Glc complexes. The mutation causes disturbances of the β-structure at the base of the handle (A), which results in the lack of closure in the SB loop region (B).

resolution of 1.6 Å. The postreactive state is the most compact of all known published[19] and herein presented structures of LmUGP. Both the accessible surface area of the protein and the distances between key structural elements and the catalytic center were at their minimum in this state, whereas the torsional deformation of the β-sheet increased (Figure 2B). Compared with the UTP-state structure, the NB loop is shifted ~2 Å closer toward the phosphate moiety, further bounding the nucleotide pocket (Figure 2C). The region R249−Y302 is in its closed state, providing maximal stabilization to the glucose ring. The amino group of the strictly conserved K380 is moved 5.6 Å toward the nucleotide, and an H-bond with the α-phosphate of UDP-Glc is formed. In the crystal structure, the sulfate ion occupies the position of the γ-phosphate in the LmUGP·dUpCpp complex. The identified magnesium ion coordinated sulfate, α-phosphate, and a water molecule. This water occupied the space between the α- and γ-phosphates and was additionally coordinated by an H-bond and electrostatic interactions with G86 and K95 of the NB loop. Superposition of the UTP and postreactive state structures suggested that in the prereactive

state, the magnesium should be coordinated between the α- and β-phosphates of UTP (Supporting Information Figure S4). Of note, with the crystal structure of the postreactive state of LmUGP, we present the first experimental structure in which the binding sites of all UGP products could be identified.

Comparison of the crystal structures of LmUGP in the postreactive and the UDP-Glc-bound states revealed that dissociation of the pyrophosphate and magnesium leads to a significant change in the NB loop conformation (Figure 5). The
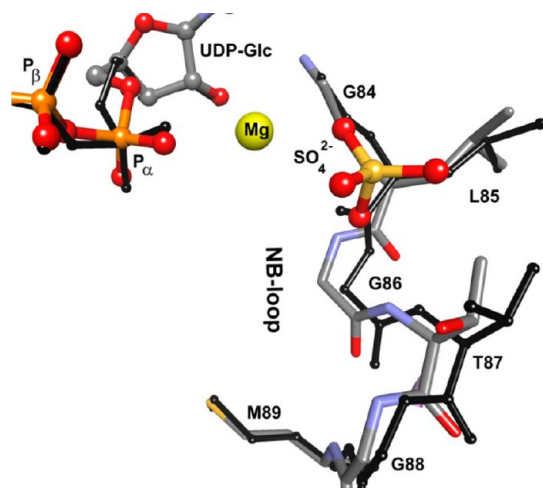

Figure 5. Experimental LmUGP crystal structures representing the postreactive (colored) and UDP-Glc (black) states. The superposition reveals conformational changes of the NB loop and phosphate moiety of UDP-Glc caused by the dissociation of pyrophosphate and Mg^{2+}.

G84−G88 residues and the adjacent G90−D93 region moved away from the active site, making it less compact. Because of the loss of the hydrogen bond with the γ-phosphate, the carbonyl group of the L85 peptide bond was flipped in the UDP-Glc state. As a result, the NB loop acquired an intermediate conformation between those of postreactive and apo states. In the crystal structure of the UDP-Glc state, the experimental electron density for this region was weaker and more disordered than that in the postreactive state (20% decrease in the signal-to-noise ratio for C_α atoms). A similar effect was observed for the SB loop residues, where destabilization led to a partial opening of the structure in the area of helix α11 (residues M293−N300) located at the end of the region R249−Y302. This destabilization effect is propagated from the NB to the SB loop via the shift of G88, which moves the conserved K422 (C-terminal domain) closer toward K255 (SB loop) and, thus, increases the electrostatic repulsion between the two regions.

The flexible top part of the handle, including residues Y265−K277 that are located farther away from the protein globule and not stabilized by intramolecular interactions, is differently structured in the postreactive and the UDP-Glc states. The lack of electron density for Mg^{2+} in the UDP-Glc complex suggests that the ion dissociates together with the pyrophosphate. The phosphate moiety of UDP-Glc also undergoes a conformational change upon dissociation of Mg^{2+} and the PP_i (Figure 5). In the UDP-Glc state, the C5*−O5* bond connecting the α-phosphate to the glucose ring is flipped 80° in comparison with the experimental geometry of the postreactive state. This change induces a shift of the K380 side chain, resulting in an increased distance between K380 and the oxygens of the α-

phosphate and, thus, in the drop of affinity for UDP-Glc. All of the above effects reveal the mechanism of unlocking the enzyme structure, which begins with the dissociation of the pyrophosphate.

Quantum Chemical Studies of LmUGP Catalysis. To study the electronic effects of UGP catalysis and identify the role of the active site residues in this process, we performed quantum chemical (QC) calculations of the LmUGP reaction pathway using the IRC procedure. The starting geometry approximation for the saddle point location search was generated using the coordinates of the protein part, the glucose ring, Mg^{2+} and water from the postreactive state complex, and the substrate coordinates from the structure of LmUGP· dUpCpp complex obtained in this work. After finding the transition state, the models of the pre- and postreactive states were obtained by descent forward and backward from the saddle point along the steepest descent path in mass-weighted Cartesian coordinates using the IRC method.[43] The overall protein conformation, the local structure of the active site residues, and the positions of nucleoside and glucose ring in the theoretical model of the LmUGP·UTP·Glc-1-P complex are very close to the experimental geometry of the postreactive state (r.m.s.d. = 1.2 Å; Figure 1C). This is in agreement with the principle of least motion in chemical reactions.[44] In the model, the phosphate moiety of UTP is structured similarly to that of the crystal structure of the LmUGP·dUpCpp complex (r.m.s.d. = 0.3 Å), whereas the phosphate group of Glc-1-P is oriented toward the α-phosphate of UTP, with a closest distance of 2.8 Å between the reagents. H191 and K380 stabilize the orientation of the Glc-1-P phosphate with hydrogen bonds, ensuring an optimal position of the attacking oxygen with respect to the α-phosphate of UTP. In this position, the highest occupied molecular orbital (HOMO) localized on the attacking oxygen O_{3P} of Glc-1-P overlaps with the lowest unoccupied molecular orbital (LUMO) localized on the P_α atom of UTP, providing an electron exchange between the reactants (Figure 1C). Atomic partial charges resulting from Mulliken population analysis[45] reveal a significant electrostatic component to this interaction.

Importantly, the QC analysis showed that the magnesium ion coordinated by the oxygen atoms of the UTP α-phosphate affects both the partial charge distribution between the reacting atoms and the local geometry of the reaction center. Comparison of the QC prereactive state models with and without Mg^{2+} revealed that the Mulliken charges on P_α^{UTP} and $O_{3P}^{Glc-1-P}$ change from +1.4 and −0.7 in the presence of Mg^{2+} to +1.15 and −0.6 in the absence of Mg^{2+}, respectively. Thus, Mg^{2+} increases the polarization and electrostatic attraction of the reacting atoms. The involvement of $O_{1\alpha}$ and $O_{3\alpha}$ of the UTP α-phosphate in the coordination sphere of Mg^{2+} imposes a flattening effect of 10° on the α-phosphate geometry, rendering it closer to the transition state. In the presence of Mg^{2+}, the covalent bond P_α^{UTP}−$O_{3\alpha}^{UTP}$ of the leaving group is elongated by 0.2 Å compared with that of the Mg^{2+}-free prereactive state, making dissociation along this bond easier. In contrast, however, the positioning, mutual orientation, and overall conformation of the reagents do not depend on Mg^{2+}, but are defined primarily by the protein matrix.

These data explain why in previous studies Mg^{2+} was shown to have a pronounced activation effect on UGPs[9] but is dispensable for nucleotide binding.[46] Analysis of the potential energy profile along the UGP reaction coordinate revealed one barrier between the pre- and postreactive states. On the top of

the barrier, the UTP α-phosphate acquires a trigonal bipyramidal configuration with a planar $P_\alpha O_3$ group and the axial coordination sites occupied by the bridging $P_\alpha - O_{3\alpha} - P_\beta$ oxygen of UTP and the attacking oxygen from Glc-1-P phosphate (Figure 1D). The angle $O_{3P}^{\text{Glc-1-P}} - P_\alpha^{\text{UTP}} - O_{3\alpha}^{\text{UTP}}$ is increased from 160° in the prereactive state to 167° in the transition state. The movement of the attacking oxygen toward P_α^{UTP} is accomplished via rotational degrees of freedom of the Glc-1-P phosphate group. The elongation of the $P_\alpha^{\text{UTP}} - O_{3\alpha}^{\text{UTP}}$ bond leads to a shift of the $P_\beta - P_\gamma$ phosphates and Mg^{2+} toward the NB loop, inducing a small adjustment of the protein main chain around G86. K380, coordinating both Glc-1-P phosphate and UTP α-phosphate, shifts in the transition state toward the α-phosphate and stabilizes the planar conformation of the $P_\alpha O_3$ group. In addition, the length of the hydrogen bond between K95 and the $O_{3\beta}^{\text{UTP}}$ oxygen is decreased in the transition state, providing more stability to the position of the β-phosphate. The tightening of the contacts among K380, K95, and the phosphate moiety of UTP enhances the affinity of the enzyme for the transition state and helps to compensate for the increased atomic charges in the penta-coordinated intermediate. The positions of other residues, including H191 that coordinates the Glc-1-P phosphate, remain unchanged between the transition and prereactive states. Together, these results show that strictly conserved positively charged residues in the active site contribute to catalysis via electrostatic stabilization of the transition state, consistent with the loss of activity in K95A and K380A mutants.[19]

In agreement with an S_N2 associative mechanism, the formation of a penta-coordinated intermediate is followed by the stereochemical inversion of the α-phosphate, the breaking of the $P_\alpha^{\text{UTP}} - O_{3\alpha}^{\text{UTP}}$ bond, and generation of a leaving pyrophosphate group and UDP-Glc. The resulting theoretical model of the postreactive UGP·UDP-Glc·Mg^{2+}·PP_i complex and its crystal structure show close similarity (r.s.m.d. 1.2 Å) (Figure 1E). According to the model, the pyrophosphate binds into a pocket created by the NB loop residues G84—T87. There, it is coordinated by hydrogen bonds with the main-chain atoms of L85 and G86, the side chain of K95, and a number of van der Waals interactions. In the crystal structure, the positions of the γ- and β-phosphates are occupied by the sulfate ion and a water molecule, respectively. In both experimental and theoretical models, Mg^{2+} is coordinated between the α, β, and γ phosphates or their analogs in a similar way. Inversion of the α-phosphate and separation of PP_i induce small shifts of the H191, K380, and K95 side chains and the main chain of the NB loop. The frontier molecular orbitals in this state are localized on $O_{3\alpha}^{PPi}$ (HOMO) and $P_\alpha^{\text{UDP-Glc}}$ (LUMO), which also represents the prereactive state of the backward reaction (Figure 1E). The distance between $O_{3\alpha}^{PPi}$ and $P_\alpha^{\text{UDP-Glc}}$ is 0.5 Å longer compared with the reacting atoms of the UGP·UTP·Glc-1-P complex. The reaction pathway calculations predict the free energy barriers for the forward and backward reactions to be 20.8 and 22.2 kcal/mol, respectively (Supporting Information Figure S3). The corresponding values derived from the experimental specific activities V_{max} at a physiological temperature of 37 °C (Supporting Information Figure S2A,B) are 20.4 and 20.6 kcal/mol (experimental details are given in the Supporting Information). Thus, the reaction energy parameters produced in the calculated model are in a good agreement with the experimental kinetics data and reproduce the observed trend for the lower activation barrier in the forward reaction.

Our study demonstrates that the interaction of K95 with the β-phosphate is important to direct the pyrophosphate to its exit channel.

■ DISCUSSION

The data presented in this manuscript filled critical gaps in the knowledge of the LmUGP mechanism and allowed a complete reconstruction of the enzymatic cycle. In the forward reaction, the working cycle of LmUGP consists of five stages: closing (activated by UTP binding), locking (initiated by Glc-1-P binding), the enzyme-catalyzed chemical reaction, unlocking (activated by pyrophosphate dissociation), and opening (coupled with UDP-Glc dissociation).

LmUGP closing is activated by UTP, whose binding site already exists in the open state. The primary role of the nucleoside in UTP binding is supported by our structure of LmUGP H191L mutant, and the crucial role of the UTP γ-phosphate in the activation mechanism is elucidated by the structure of the LmUGP·dUpCpp complex. The activation effect of the γ-phosphate involves the large shift of the NB loop, which in its turn is bound to both the C-terminal domain and the seven-stranded β-sheet (Figure 2B). This shift causes conformational changes in these areas, particularly a torsional deformation of the β-sheet. The latter leads to a formation of the allosteric binding site for the second substrate. With this definition of the role of the γ-phosphate in the allosteric mechanism of LmUGP activation, our structure explains the previous findings[2] that UDP and UMP, lacking the γ-phosphate, are not able to activate LmUGP for the binding of the second substrate, Glc-1-P.

Binding of the second substrate initiates further changes in the LmUGP structure. The structural and kinetic data obtained with the mutants E284A and L281D strongly suggest that the UTP-induced torsional deformation of the β-sheet allows the glucose ring to be prepositioned in its binding site so that the interaction between the O2′ and O3′ hydroxyls of glucose and the carboxyl of E284 can occur. This interaction pulls the adjacent area of the handle, the SB loop and helix α11 toward the C-terminal domain, which stabilizes the Glc-1-P binding site, brings strictly conserved H191 and K380 to favorable positions for phosphate binding, and closes the LmUGP structure. Thus, E284 is playing a primary role in the process of glucose stabilization by LmUGP (as reflected by the >6-fold decrease in Glc-1-P affinity in the E284A mutant, Supporting Information Figure S2D) while the SB loop plays a secondary role. We defined this mechanism of the second substrate stabilization as "the lock mechanism" and the residues R249—Y302 as "the lock region" (Figure 1). The locking is facilitated by the base of the handle, which acts as a transducer of tensile force from E284 to the SB loop. The detailed allosteric mechanism of the lock was revealed by molecular dynamics simulations and confirmed by our kinetic and structural studies of LmUGP mutants.

Torsional deformation of the β-sheet and conformational changes in the lock area provide new insights into the mechanism of specific recognition of the second substrate by LmUGP.[2] Superposition of the LmUGP·UDP-Glc·Mg^{2+}·SO_4 complex (postreactive state) with the LmUSP·UDP-Gal complex[47] (a promiscuous UDP-sugar pyrophosphorylase) showed that the main steric hindrance preventing the binding of galactose by LmUGP is caused by the main chain of N306 (β11). N306 belongs to the area where the torsional deformation of the β-sheet reaches its maximum. In LmUSP,

the torsional deformation of the β-sheet is of a lesser magnitude, which leaves more space to accommodate unspecific sugars. This observation indicates that the specificity for the second substrate in nucleotidyltransferases can be controlled via allosteric mechanisms.

Binding and stabilization of both substrates brings LmUGP to the most compact state optimal for the catalytic reaction. Our ab initio QM/MM calculations of the LmUGP reaction pathway displayed the chemical conditions for the start of the reaction, elucidated the role of each residue in the catalytic center during the reaction and explained the observed necessity of Mg^{2+} for catalysis[9] but not for the nucleotide binding.[46] The LmUGP catalysis involves the proximity and orientation effect provided by the active site protein matrix, bond strain and electrostatic activation by the magnesium cofactor, and electrostatic stabilization of the transition state by the positively charged residues K380 and K95. The latter is also playing an important role in directing the pyrophosphate to its exit channel. With this, we provide a molecular explanation for the previously hypothesized role of the positively charged active site residues in guiding the PP_i release.[11]

The structural models and reaction free energy barriers for the forward and backward reactions obtained from the QC calculations were in a good agreement with experimental data. The position of Mg^{2+} in the experimental postreactive state structure and in the QC models of LmUGP is similar to that in the structure of bacterial guanosine–diphospho-D-mannose pyrophosphorylase (GMP)[48] in complex with GTP (pdb code: 2X60) and to one of the two observed Mg^{2+} positions in the complex of UGP from *Corynebacterium glutamicum* with UDP-Glc[49] (pdb code: 2PA4). It is interesting that in the latter structure as well as in the complex of GMP with GDP-Man[48] (pdb code: 2X5Z), the catalytically important Mg^{2+} occupies another position that coincides with the position of the K380 amino group in LmUGP (Supporting Information Figure S4). Despite the different position, the Mg^{2+} in all structures includes the α-phosphate group in its coordination sphere and imposes similar distortions on the α-phosphate geometry as defined in LmUGP. On the basis of this finding, it can be concluded that, independent of the binding mode of Mg^{2+} in the different nucleotidyltransferases, its mechanism of substrate activation remains the same.

The high-resolution crystal structure of the postreactive state showed for the first time the binding sites of all UGP products and allowed revealing the mechanism of unlocking the enzyme after the reaction. The unlocking is initiated by dissociation of the pyrophosphate and Mg^{2+} ions. This causes the destabilization of the NB loop and the lock region as well as a conformational change of the UDP-Glc phosphate moiety, thus activating the structure for closed-to-open transition. The full opening of the enzyme should then be coupled with the dissociation of UDP-Glc with the glucose part dissociating first. It is of note to mention that we could confirm this reaction sequence in a later structural study of human UGP (manuscript in preparation).

The mechanisms of catalysis and allosteric regulation of LmUGP as described in this work should significantly facilitate investigations of the reaction cycles and allosteric regulation networks of other nucleotidyltransferases that also follow ordered sequential Bi Bi kinetics. Moreover, our data help one to understand the coupling between global conformational changes and events at the active site during the reaction of these enzymes. This information would be particularly useful for drug-design applications utilizing nucleotidyltransferases as drug targets. Structural similarities of nucleotidyltransferases make targeting their active sites likely to cause unwanted, unspecific disruption of enzymatic pathways in the host. A solution to this problem can be provided by employing allosteric effects in the drug-design strategy, utilizing the conformational control by nonconserved residues located far from the catalytic center. A comprehensive description of the enzymatic mechanism and allosteric effects would thus be an important prerequisite for rational development of highly specific allosteric regulators for these enzymes.

Finally, our structural and kinetic data on the L281D mutant as well as computational analysis reveal the mechanism of mechanical control of the chemical reaction in the active site of LmUGP. This mechanism involves the tensile force transduction between the strictly conserved residue E284 and the SB loop via the β-structure of the handle. Decreasing the efficiency of the force transduction by disturbing the β-structure leads to the loss in specific activity of the enzyme, as demonstrated by the L281D mutation. This illustrates how regulating the efficiency of mechanical force transduction in allosteric chains could be used to alter the catalytic activity in allosteric enzymes. Small molecule compounds producing similar effects could be used in drug design and biotechnological applications. The concept of mechanical regulation of enzymatic and homogeneous chemical catalysts has attracted attention as a result of its potential applications in biotechnology[50−52] and new functional materials.[53] Studying natural evolutionarily optimized mechanisms of such regulation, as in the case of LmUGP, can have a strong impact on the development of artificial mechanochemical catalysts.

■ ASSOCIATED CONTENT

Ⓢ Supporting Information

Crystallographic data and refinement statistics, experimental electron density omit maps, kinetic data, reaction energy diagram, and superposition of the active sites of nucleotidyltransferases. This information is available free of charge via the Internet at http://pubs.acs.org/

Accession Codes

Coordinates for the structures LmUGPwt·UDP-Glc·Mg·SO$_4$, LmUGP$_{L281D}$·UDP-Glc, LmUGP$_{H191L}$, and LmUGPwt·dUpCpp have been deposited in the Protein Data Bank with the accession codes 4M2A, 4M2B, 4J18, and 4M28, respectively.

■ AUTHOR INFORMATION

Corresponding Author

*Phone: +49-5115323705. Fax: +49-5115325966. E-mail: Fedorov.Roman@mh-hannover.de.

Present Address

⊥(A.-C.L.) Roche Diagnostics GmbH, Sandhofer Strasse 116, 68305 Mannheim, Germany.

Notes

The authors declare no competing financial interest.

■ ACKNOWLEDGMENTS

X11 and X13 at DESY/EMBL-Hamburg and beamlines ID23 and ID29 at the ESRF/Grenoble for their support during diffraction data collection. This study received financial support from the European Community's Seventh Framework Programme (FP7/2007−2013; grant agreement No. 226716), the German Research Foundation in the frame of the Cluster of Excellence REBIRTH, and an intramural grant ("HiLF") of Hannover Medical School. The funders had no role in study design, data collection and analysis, decision to publish, or preparation of the manuscript.

■ REFERENCES

(1) Kuchta, K.; Knizewski, L.; Wyrwicz, L. S.; Rychlewski, L.; Ginalski, K. *Nucleic Acids Res.* **2009**, *37*, 7701−7714.

(2) Lamerz, A. C.; Haselhorst, T.; Bergfeld, A. K.; von Itzstein, M.; Gerardy-Schahn, R. *J. Biol. Chem.* **2006**, *281*, 16314−16322.

(3) Kleczkowski, L. A.; Martz, F.; Wilczynska, M. *Phytochemistry* **2005**, *66*, 2815−2821.

(4) Blankenfeldt, W.; Asuncion, M.; Lam, J. S.; Naismith, J. H. *EMBO J.* **2000**, *19*, 6652−6663.

(5) Koropatkin, N. M.; Cleland, W. W.; Holden, H. M. *J. Biol. Chem.* **2005**, *280*, 10774−10780.

(6) Roeben, A.; Plitzko, J. M.; Korner, R.; Bottcher, U. M.; Siegers, K.; Hayer-Hartl, M.; Bracher, A. *J. Mol. Biol.* **2006**, *364*, 551−560.

(7) Sivaraman, J.; Sauve, V.; Matte, A.; Cygler, M. *J. Biol. Chem.* **2002**, *277*, 44214−44219.

(8) Jin, X.; Ballicora, M. A.; Preiss, J.; Geiger, J. H. *EMBO J.* **2005**, *24*, 694−704.

(9) Turnquist, R. L.; Gillett, T. A.; Hansen, R. G. *J. Biol. Chem.* **1974**, *249*, 7695−7700.

(10) Barton, W. A.; Lesniak, J.; Biggins, J. B.; Jeffrey, P. D.; Jiang, J.; Rajashankar, K. R.; Thorson, J. S.; Nikolov, D. B. *Nat. Struct. Biol.* **2001**, *8*, 545−551.

(11) Zuccotti, S.; Zanardi, D.; Rosano, C.; Sturla, L.; Tonetti, M.; Bolognesi, M. *J. Mol. Biol.* **2001**, *313*, 831−843.

(12) Ballicora, M. A.; Iglesias, A. A.; Preiss, J. *Photosynth. Res.* **2004**, *79*, 1−24.

(13) Martinez, L. I.; Piattoni, C. V.; Garay, S. A.; Rodrigues, D. E.; Guerrero, S. A.; Iglesias, A. A. *Biochimie* **2011**, *93*, 260−268.

(14) Smith, T. L.; Rutter, J. *Mol. Cell* **2007**, *26*, 491−499.

(15) Ballicora, M. A.; Iglesias, A. A.; Preiss, J. *Microbiol. Mol. Biol. Rev.* **2003**, *67*, 213−225.

(16) Martz, F.; Wilczynska, M.; Kleczkowski, L. A. *Biochem. J.* **2002**, *367*, 295−300.

(17) Macrae, J. I.; Obado, S. O.; Turnock, D. C.; Roper, J. R.; Kierans, M.; Kelly, J. M.; Ferguson, M. A. *Mol. Biochem. Parasitol.* **2006**, *147*, 126−136.

(18) Urbaniak, M. D.; Tabudravu, J. N.; Msaki, A.; Matera, K. M.; Brenk, R.; Jaspars, M.; Ferguson, M. A. J. *Bioorg. Med. Chem. Lett.* **2006**, *16*, 5744−5747.

(19) Steiner, T.; Lamerz, A. C.; Hess, P.; Breithaupt, C.; Krapp, S.; Bourenkov, G.; Huber, R.; Gerardy-Schahn, R.; Jacob, U. *J. Biol. Chem.* **2007**, *282*, 13003−13010.

(20) Damerow, S.; Lamerz, A. C.; Haselhorst, T.; Fuhring, J.; Zarnovican, P.; von Itzstein, M.; Routier, F. H. *J. Biol. Chem.* **2010**, *285*, 878−887.

(21) Kabsch, W. *Acta Crystallogr., Sect. D: Biol. Crystallogr.* **2010**, *66*, 125−132.

(22) Winn, M. D.; Ballard, C. C.; Cowtan, K. D.; Dodson, E. J.; Emsley, P.; Evans, P. R.; Keegan, R. M.; Krissinel, E. B.; Leslie, A. G.; McCoy, A.; McNicholas, S. J.; Murshudov, G. N.; Pannu, N. S.; Potterton, E. A.; Powell, H. R.; Read, R. J.; Vagin, A.; Wilson, K. S. *Acta Crystallogr., Sect. D: Biol. Crystallogr.* **2011**, *67*, 235−242.

(23) Navaza, J. *Acta Crystallogr., Sect. A: Found. Crystallogr.* **1994**, *A50*, 157−163.

(24) Brunger, A. T. *Nat. Protoc.* **2007**, *2*, 2728−2733.

(25) Brunger, A. T.; Adams, P. D.; Clore, G. M.; DeLano, W. L.; Gros, P.; Grosse-Kunstleve, R. W.; Jiang, J. S.; Kuszewski, J.; Nilges, M.; Pannu, N. S.; Read, R. J.; Rice, L. M.; Simonson, T.; Warren, G. L. *Acta Crystallogr., Sect. D: Biol. Crystallogr.* **1998**, *54*, 905−921.

(26) Sheldrick, G. M. *Acta Crystallogr., Sect. A: Found. Crystallogr.* **2008**, *64*, 112−122.

(27) Murshudov, G. N.; Vagin, A. A.; Dodson, E. J. *Acta Crystallogr., Sect. D: Biol. Crystallogr.* **1997**, *53*, 240−255.

(28) Perrakis, A.; Sixma, T. K.; Wilson, K. S.; Lamzin, V. S. *Acta Crystallogr., Sect. D: Biol. Crystallogr.* **1997**, *53*, 448−455.

(29) Emsley, P.; Lohkamp, B.; Scott, W. G.; Cowtan, K. *Acta Crystallogr., Sect. D: Biol. Crystallogr.* **2010**, *66*, 486−501.

(30) Schroder, G. F.; Levitt, M.; Brunger, A. T. *Nature* **2010**, *464*, 1218−1222.

(31) Granovsky, A. A. *Firefly*; 2009.

(32) Schmidt, M. W.; Baldridge, K. K.; Boatz, J. A.; Elbert, S. T.; Gordon, M. S.; Jensen, J. H.; Koseki, S.; Matsunaga, N.; Nguyen, K. A.; Su, S.; Windus, T. L.; Dupuis, M.; Montgomery, J. A. *J. Comput. Chem.* **1993**, *14*, 1347−1363.

(33) Becke, A. D. *J. Chem. Phys.* **1993**, *98*, 5648−5652.

(34) Lee, C.; Yang, W.; Parr, R. G. *Phys. Rev. B: Condens. Matter Mater. Phys.* **1988**, *37*, 785−789.

(35) Vosko, S. H.; Wilk, L.; Nusair, M. *Can. J. Phys.* **1980**, *58*, 1200−1211.

(36) Stephens, P. J.; Devlin, F. J.; Chabalowski, C. F.; Frisch, M. J. *J. Phys. Chem.* **1994**, *98*, 11623−11627.

(37) Lii, J. H.; Allinger, N. L. *J. Am. Chem. Soc.* **1989**, *111*, 8566−8575.

(38) Allinger, N. L.; Yuh, Y. H.; Lii, J. H. *J. Am. Chem. Soc.* **1989**, *111*, 8551−8566.

(39) Lii, J. H.; Allinger, N. L. *J. Am. Chem. Soc.* **1989**, *111*, 8576−8582.

(40) Baker, J. *J. Comput. Chem.* **1986**, *7*, 385−395.

(41) Helgaker, T. *Chem. Phys. Lett.* **1991**, *182*, 503−510.

(42) Culot, P.; Dive, G.; Nguyen, V. H.; Ghuysen, J. M. *Theor. Chim. Acta* **1992**, *82*, 189−205.

(43) Gonzalez, C.; Schlegel, H. B. *J. Chem. Phys.* **1989**, *90*, 2154−2161.

(44) Hine, J. *Adv. Phys. Org. Chem.* **1977**, *15*, 1−61.

(45) Mulliken, R. S. *J. Chem. Phys.* **1955**, *23*, 1833−1840.

(46) Stevens, R. A. J.; Phelps, C. F. *Biochem. J.* **1976**, *159*, 65−70.

(47) Dickmanns, A.; Damerow, S.; Neumann, P.; Schulz, E. C.; Lamerz, A. C.; Routier, F. H.; Ficner, R. *J. Mol. Biol.* **2011**, *405*, 461−478.

(48) Pelissier, M. C.; Lesley, S. A.; Kuhn, P.; Bourne, Y. *J. Biol. Chem.* **2010**, *285*, 27468−27476.

(49) Thoden, J. B.; Holden, H. M. *Protein Sci.* **2007**, *16*, 1379−1388.

(50) Choi, B.; Zocchi, G.; Wu, Y.; Chan, S.; Jeanne, P. L. *Phys. Rev. Lett.* **2005**, *95*, 078102.

(51) Saghatelian, A.; Guckian, K. M.; Thayer, D. A.; Ghadiri, M. R. *J. Am. Chem. Soc.* **2003**, *125*, 344−345.

(52) Choi, B.; Zocchi, G.; Canale, S.; Wu, Y.; Chan, S.; Perry, L. J. *Phys. Rev. Lett.* **2005**, *94*, 038103.

(53) Piermattei, A.; Karthikeyan, S.; Sijbesma, R. P. *Nat. Chem.* **2009**, *1*, 133−137.